Heat losses in ATES systems

The impact of processes, storage geometry and temperature

Beernink, Stijn; Hartog, Niels; Vardon, Philip J.; Bloemendal, Martin

Important note
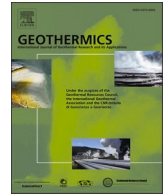To cite this publication, please use the final published version (if applicable).
Please check the document version above.

Heat losses in ATES systems: The impact of processes, storage geometry and temperature

Stijn Beernink [a,b,*], Niels Hartog [a,c], Philip J. Vardon [b], Martin Bloemendal [a,b]

[a] *KWR water research institute, Nieuwegein, the Netherlands*
[b] *Delft University of Technology, Delft, the Netherlands*
[c] *Faculty of Geosciences, Utrecht University, Utrecht, the Netherlands*

ABSTRACT

The technical and economic success of an Aquifer Thermal Energy Storage (ATES) system depends strongly on its thermal recovery efficiency, i.e. the ratio of the amount of energy that is recovered to the energy that was injected. Typically, conduction most strongly determines the thermal recovery efficiency of ATES systems at low storage temperatures (<25 °C), while the impact of buoyancy-driven flow can lead to high additional heat losses at high storage temperatures (>50 °C). To date, however, it is unclear how the relative contribution of these processes and mechanical dispersion to heat losses across a broad temperature range is affected by their inter-action for the wide range of storage conditions that can be encountered in practice. Since such process-based insights are important to predict ATES performance and support the design phase, numerical thermo-hydraulic ATES simulations were conducted for a wide range of realistic operational storage conditions ([15–90 °C], [50,000–1,000,000 m^3/year]) and hydrogeological conditions (aquifer thickness, horizontal hydraulic conductivity, anisotropy). The simulated heat loss fractions of all scenarios were evaluated with respect to analytical solutions to assess the contribution of the individual heat loss processes. Results show that the wide range of heat losses (10–80 % in the 5th year) is the result of varying contributions of conduction, dispersion and buoyancy-driven flow, which are largely determined by the geometry of the storage volume (ratio of screen length / thermal radius, L/R_{th}) and the potential for buoyancy-driven flow (q_0) as affected by the storage temperature and hydraulic conductivity of the aquifer. For ATES systems where conduction dominates the heat losses, a L/R_{th} ratio of 2 minimizes the thermal area over volume ratio (A/V) and resulting heat losses for a given storage volume. In contrast however, the impact of dispersion decreases with L/R_{th} and particularly for ATES systems with a high potential for buoyancy-driven flow ($q_0 > 0.05$ m/d), increasingly smaller L/R_{th} ratios (<1) strongly reduce the heat losses due to tilting. Overall, the results of this study support the assessment of thermal recovery efficiencies for particular aquifer and storage conditions, thereby aiding the optimization of initial ATES designs.

1. Introduction

The reduction of greenhouse gas (GHG) emissions to limit the increasing impact of climate change is an important global challenge in the coming decades. One of the major contributors to GHG emissions is the use of fossil fuels for heating and cooling purposes, accountable for ~40 % of global energy end-use between 2015 and 2019 (IEA, 2019; Ürge-Vorsatz et al., 2015). Many alternative sustainable and low GHG emission sources of heat exist (e.g. geothermal heat, solar heat collectors, power-to-heat systems) and their contribution to the energy system is projected to increase strongly in the coming decades. However, there

is generally a temporal mismatch in the availability of heat from such sources and consumer demand, mainly on a seasonal basis. Depending on subsurface conditions and storage requirements, subsurface storage techniques, e.g. Borehole Thermal Energy Storage (BTES) and Aquifer Thermal Energy Storage (ATES), make these renewable heating systems more autonomous, efficient and cost-effective (Kallesøe and Vangkil-de-Pedersen, 2019). As a consequence, the interest in aquifer thermal energy storage (ATES) systems to provide large-scale seasonal storage is rising (Dincer, 2002; Henry et al., 2020; van der Roest et al., 2021). While ATES is currently mostly applied at low temperatures (LT-ATES < 25 °C) in conjunction with a heat pump to boost heating temperatures,

---

storage at higher temperatures (HT-ATES, typically up to 90 °C) provides strong GHG reduction potential for large scale and direct use of renewable heat (Daniilidis et al., 2022; Fleuchaus et al., 2018; Wesselink et al., 2018).

The technical and economic success of any ATES system depends on the thermal recovery efficiency (η) of heat from its wells, i.e. the ratio of the amount of energy that is recovered to the energy that was injected. Three intrinsic thermo-hydraulic processes impact the thermal recovery efficiency for any ATES well: conduction, dispersion and buoyancy-driven flow (Buscheck et al., 1983; Doughty et al., 1982). Previous studies showed that conduction and dispersion are important for low temperature wells (Bloemendal and Hartog, 2018; Doughty et al., 1982) and that at high storage temperatures relative to the ambient groundwater temperature, buoyancy-driven flow can considerably impact the performance (Buscheck et al., 1983; van Lopik et al., 2016). Recently, methods have been developed that assess the ratio of conduction versus buoyancy-driven flow and empirically estimate the thermal recovery efficiency of ATES wells at high storage temperature (Schout et al., 2014; Sheldon et al., 2021). Although these studies show that ATES performance is more variable at higher storage temperatures, their use for a wide range of storage temperatures and storage conditions is uncertain. To get insight in the applicability of ATES at low to high storage temperatures, it is important to know which processes are dominating for varying conditions and how they together impact well performance for relevant practical conditions. However, it is yet to be quantified how conduction, dispersion and buoyancy-driven flow occur simultaneously and together lead to heat losses for a wide range of storage temperatures and storage conditions. Guidelines and insights to identify suitable conditions for low to high temperature ATES are currently lacking, resulting in uncertainties regarding its feasibility.

Therefore, this study addresses the relative contribution of conduction, dispersion and buoyancy-driven flow to ATES well heat losses under various storage conditions and low to high storage temperatures, and further examines how ATES design could be optimized accordingly. The following approach is used: Firstly, ATES well performance is assessed and quantified using a structured sensitivity analysis varying storage conditions using a numerical model. The results of the sensitivity analysis are then benchmarked and compared with analytical solutions derived in this study and from literature. The results from this study provide key insights to understand how the different processes contribute to heat losses of ATES and foster subsurface design in practice.

2. Methods and materials

2.1. Theory

ATES systems utilize tubular well doublets to simultaneously extract and inject groundwater at different temperatures (Bloemendal and Hartog, 2018). The well screens, where groundwater is injected and extracted, are preferably installed through the entire thickness of the aquifer, between two hydrologically impermeable layers at the top and the bottom. During injection, thermal energy is transported into the aquifer around the tube well via advective flow. The sensible heat, that is initially contained in the injected water volume, is partly absorbed by the solid aquifer material. Hence, the thermal radius of the stored hot cylinder is smaller than the hydraulic radius of the injected volume (the thermal radius is about two-thirds of the radial distance that the water travels (Bloemendal and Hartog, 2018)). For an idealized well, i.e. fully penetrating well screen, homogenous aquifer conditions and no losses, the thermal radius (R_{th}) can be defined as (Bloemendal and Hartog, 2018):

$$R_{th} = \sqrt{\frac{c_w V_{in}}{c_{aq} \pi L}} \tag{1}$$

where V_{in} is the stored groundwater volume (m^3), L the aquifer thickness (m), c_w and c_{aq} the volumetric heat capacity of water and the bulk aquifer respectively (J/m^3/°C). As is common for ATES studies (Sommer et al., 2014), the bulk volumetric heat capacity of the aquifer is calculated as the porosity weighed average of the volumetric heat capacity of the solids and the water (Table 1).

2.1.1. Thermal storage geometry of ATES wells

As a result of well injection and extraction, the storage geometry associated with an ATES well changes during each part of the annual cycle. The thermal radius of an ATES well increases during charging, and is at the maximum radius at the end of the charging and during the storage period and decreases again during the discharge phase (Fig. 1).

Heat losses occur at the surface area between the volume of stored heated groundwater and the ambient groundwater, making the size of these surfaces important for energy performance analysis (Fig. 1, Fig. 2). As the thermal radius increases during injection, both the surface area towards the aquitards ($A_{aquitard}$) and the surface area into the aquifer ($A_{aquifer}$) increase. The rate of increase differs, as the radial area ($A_{aquifer}$) increases linearly with the thermal radius ($2 \cdot \pi \cdot R_{th} \cdot L$), while the surface area to the top and bottom increases quadratically ($2 \cdot \pi \cdot R_{th}^2$). The relative area of $A_{aquifer}$ compared to the $A_{aquitard}$ surface is equal to L/R_{th}:

$$\frac{2\pi R_{th} L}{2\pi R_{th}^2} = \frac{L}{R_{th}} \tag{2}$$

Similarly to the ratio of L/R_{th}, another storage geometry parameter that is used in this study is the total thermal surface area (A_{th}), divided by the total stored thermal volume (V_{th}) (Bloemendal and Hartog, 2018):

$$\frac{A_{th}}{V_{th}} = \frac{2}{L} + \frac{2}{R_{th}} \tag{3}$$

For simplicity and convenient notation, A_{th}/V_{th} is described as A/V in this paper. Both the L/R_{th} and A/V ratio are used to relate the impact of the storage geometry on heat losses. The A/V, for a given storage volume, is smallest when the ratio of L/R_{th} is equal to 2, meaning that the diameter of the cylindrical thermal storage volume is equal to its height (Bloemendal and Hartog, 2018; Doughty et al., 1982).

2.1.2. Heat losses

Heat (or thermal) losses are considered to occur from three intrinsic processes: thermal conduction, dispersion and buoyancy-driven flow i.e. free convection due to density differences which originate from the temperature difference between the stored and ambient groundwater temperature. These processes exhibit their effect at different strength and places in the aquifer around the ATES well, depending on the

Table 1
Geohydrological and thermal properties used for the standard SEAWAT model used in this study (Bloemendal and Hartog, 2018; Caljé, 2010). The hydraulic conductivity and the longitudinal dispersion length is varied in some of the extra model scenarios.

Parameter	Symbol	Value	Unit
Porosity	n	0.3	–
Aquifer horizontal hydraulic conductivity*	K_h	Variable	m/d
Aquitard horizontal hydraulic conductivity*	K_h^{aqt}	0.05	m/d
Hydraulic conductivity anisotropy (K_h/K_v)*	γ_{ani}	5	–
Longitudinal dispersion length	α_l	0.5	m
Transversal dispersion length	α_t	0.05	m
Density solids	ρ_s	2640	kg/m^3
Specific heat capacity solid	w_s	710	J/kg/ °C
Specific heat capacity water	w_c	4183	J/kg/ °C
Thermal conductivity of aquifer material (sand)	κ_s	2	W/m/ °C
Thermal conductivity of aquitard material (clay)	κ_c	2	W/m/ °C
Thermal conductivity water	κ_w	0.58	W/m/ °C
Bulk thermal diffusivity	D	0.053	m^2/day
Ambient groundwater temperature	T_{amb}	1 2	°C

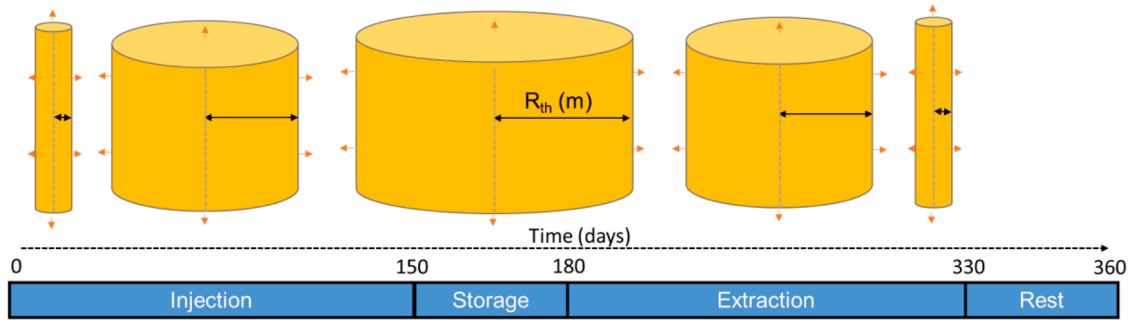* Defined at ambient groundwater temperature (12 °C).

Fig. 1. Schematic storage geometry variation of the thermal volume stored around an ATES well during one ATES cycle. In this study, the time of injection/extraction is 150 days and the time of storage and rest is 30 days. In practice, charging, storage and discharge periods may vary greatly due to variations in demand and availability of thermal energy.
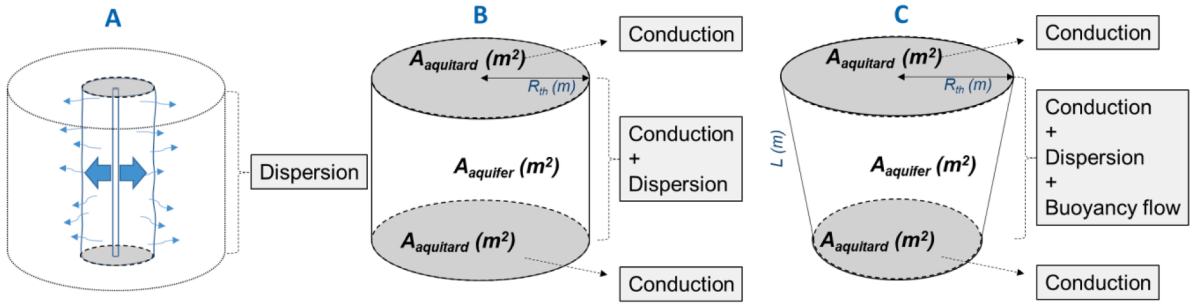

Fig. 2. Schematic overview of the intrinsic processes and the location where their effect occurs for ATES wells. A. due to variations in flow velocity, dispersion causes spreading of the temperature front, this only occurs where the groundwater flows, so across the area of the temperature front in the aquifer ($A_{aquifer}$). B. Heat conduction occurs into all directions due to the temperature difference with the ambient ground(water) into $A_{aquitard}$ and $A_{aquifer}$. C. When the temperature difference between the ambient groundwater and the stored heated groundwater is large, a density difference occurs and the thermal front may tilt due to buoyancy-driven flow, changing all associated surface areas.

storage conditions (Fig. 2). For cyclic injection and extraction of warm/cold groundwater with relatively low temperature differences, such as LT-ATES systems, heat losses have been shown to be caused by conduction and dispersion (Bloemendal and Hartog, 2018; Doughty et al., 1982). Conduction occurs because of the temperature gradient between the boundary of the stored thermal volume and ambient groundwater, and is governed by the thermal conductivity of the material according to Fourier's law. The losses due to conduction decrease with the ratio of A/V (Eq. (3)), which is minimized at $L/R_{th}=2$ for a given storage volume as shown in Fig. 4A. Dispersion occurs due to the variation in pore flow speeds due to irregularities in the matrix, both at the micro (grain) level and due to larger scale heterogeneities. Dispersion is represented by the product of the longitudinal dispersion length (α_l) and the radial flow velocity of the groundwater (Scheidegger, 1961). As the vertical flow into aquitards is negligible, there are no vertical dispersion losses into the aquitard. The flow rate is highest close to the well bore. Hence, the highest amount of dispersion is associated near the well and decreases as the thermal front moves away from the well. The combined contribution of conduction and dispersion is given by the effective thermal diffusivity (Anderson, 2005; Rau et al., 2012).

$$D_{eff} = \frac{\kappa_{aq}}{C_{aq}} + \alpha_l \left(\frac{C_w}{C_{aq}}\right) q \qquad (4)$$

where κ_{aq} is the aquifer thermal conductivity (W/m/°C), α_l is the longitudinal dispersion length (m), C_w and C_{aq} are the volumetric heat capacity of water and the bulk aquifer respectively (J/m³/°C) and q the radial velocity of the groundwater (m/s).

Buoyancy-driven flow occurs due to the buoyant forces created by density differences between lighter hot water and heavier cold water (Hellström et al., 1988a, 1988b; van Lopik et al., 2016). As buoyancy-driven flow occurs at the thermal front, the thermal front

starts to tilt, with the initial tilting rate described as a function of the so-called characteristic buoyancy flow velocity (q_0) by Hellström et al. (1988a) as follows:

$$q_0 = \frac{\sqrt{k_h k_v}\left(\rho_{amb} - \rho_{T_{inj}}\right)g}{\mu_{amb} + \mu_{T_{inj}}} \qquad (5)$$

where k_v and k_v are the horizontal and vertical intrinsic permeability (m²) of the aquifer, $(\rho_{amb} - \rho_{Tinj})$ is the density difference between the ambient and the injected groundwater (kg/m³), g is the gravitational constant (9.81 m/s) and μ_{amb} and μ_{inj} are the ambient and injected water viscosity (kg/m/s). The initial tilting rate of the thermal front (ω_0) is subsequently given by (Hellström et al., 1988a):

$$\omega_0 = \frac{32G}{\pi^2}\gamma_{ani}\frac{C_w}{C_{aq}}q_0\frac{1}{L} \qquad (6)$$

where G is Catalan's constant (~0.916), and γ_{ani} is the anisotropy factor (K_h/K_v). As water density and viscosity decreases with temperature, q_0 and ω_0 increase with temperature.

2.2. Modelling approach

2.2.1. Simulation model

Simulations are conducted using the numerical model SEAWATv4 to model the thermo-hydraulic behavior of the system. Hydraulic transport is governed by Darcy's law including the impact of variable-density and viscosity dependent flow (Langevin, 2009), with heat transport mechanisms of forced convection (due to injected/extraction of water) and natural convection (buoyancy-driven flow), conduction and dispersion. The simulation environment is setup in such a way that heat transport mechanisms can be switched on or off to discriminate between their

individual impacts. Non-linear temperature related water properties were implemented in the model for viscosity as (Voss, 1984):

$$\mu(T) = 2.494 \cdot 10^{-5} \cdot 10^{\frac{248.37}{T+133.15}} \qquad (7)$$

With T the temperature in °C. For density, the non-linear temperature dependency up to 100 °C is fitted to the relationship given in Sharqawy et al. (2012) and included in the model as:

$$\rho(T) = 1000 - \frac{(T-4)^2}{207} \qquad (8)$$

With T the temperature in °C. The simulation model was recently successfully benchmarked (Mindel et al., 2021). This simulator is a combination of MODFLOW (Harbaugh et al., 2000) and MT3DS (Zheng and Wang, 1999), in which flow and transport is simulated sequentially. FloPy is used to run and control SEAWATv4 from a python environment (Bakker et al., 2016). To minimize run time, while being able to optimize the grid discretization around the well, an axisymmetric model is used (Langevin, 2008; Vandenbohede et al., 2014).

2.2.2. Simulation set-up and parameters

The simulations consider the injection and abstraction for a single well, thus one of the two wells of an ATES doublet, in a homogeneous aquifer (Fig. 3B). It is thus assumed that the injection and abstraction in the other well of the doublet has no significant impact on the hydrostatic and thermal field of the simulated well, which is reasonable as ATES wells are in practice placed sufficiently apart, which was tested with simulations that included both wells of the ATES doublet at a distance of 3 times the thermal radius. The thickness of the aquifer is varied in different simulations and is confined by aquitards of 20 m thickness at

the top and bottom. An example of one of the simulated scenarios is shown in Fig. 3. The following conditions are applied:

- Well screens fully penetrate the injection aquifer, i.e. $L_{well} = L_{aquifer}$.
- Ambient groundwater temperature (T_{amb}) is 12 °C for all scenarios (defining the initial and boundary conditions).
- No ambient groundwater flow is considered in this study.

Ambient groundwater flow is not included in this study as Bloemendal and Hartog (2018) already provide an analytical basis to estimate the heat losses due to this process and show that the storage geometry strongly influences its potential impact. The horizontal and vertical hydraulic conductivity of the aquitards were set constant for all simulations at $K_h = 0.05$ and $K_v = 0.01$ (m/d) respectively at ambient groundwater temperature (12 °C). The values of hydraulic conductivity ("K", m/d) that are mentioned in this study represent the hydraulic conductivity at ambient groundwater temperature (12 °C). With increasing temperature in the model due to e.g. heat injection, the apparent hydraulic conductivity of the model cells accordingly increases as density and viscosity decrease with higher temperatures (Langevin et al., 2008). Isotropic properties are applied, except for the hydraulic conductivity of the aquifer which is defined as being anisotropic. The injection and extraction flow is equally distributed across the well screen length, as preliminary simulations showed only minor differences (<2 % η in year 5) for resulting thermal recovery efficiencies compared to more computationally demanding ATES models that allowed the non-uniform in/outflow to the well as a result of density and viscosity differences, for the conditions tested in this study. The horizontal model boundary (at $x \geq 2500$ m) is set at constant (hydrostatic) head and constant

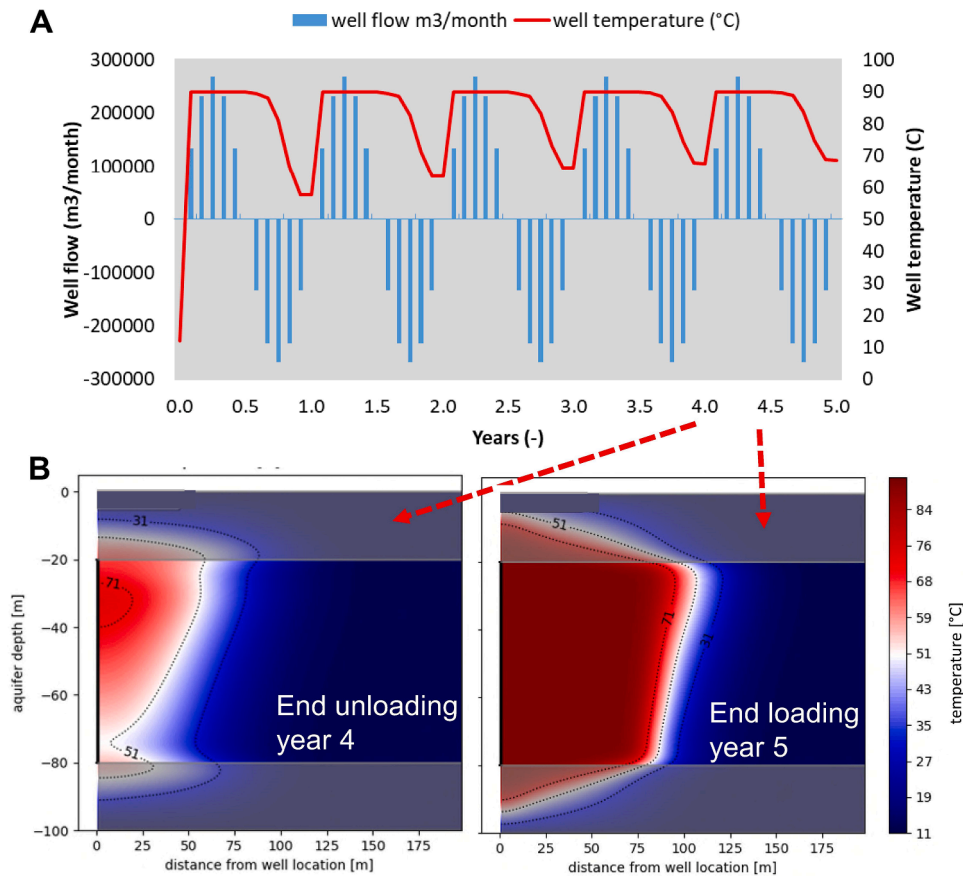**Fig. 3.** Example result of one of the modelled scenarios (storage temperature is 90 [°C] aquifer thickness = 60 [m], storage volume = 1×10^6 [m³] hydraulic conductivity (K_h & K_v) is 5 & 1 [m/d]. A. The monthly well flows and well temperature, B. Cross section along radius of the axisymmetric model. The arrows indicate the time in the fifth year that is shown in part B.

temperature (T_{amb}). The boundary conditions at the outer edge of the aquitards at the top and bottom of the model are set at constant temperature (T_{amb}) and constant head. For the modelled period of 5 cycles, preliminary simulations using thicker aquitards (40–60 m) showed no influence of the upper and lower constant temperature boundary on the performance of the ATES wells. Temporal variation in input and output flow is set at monthly time steps. The vertical cell size Δz is 0.5 m for the entire model domain. The horizontal cell size Δx is 1 m close to the well. From 100 m to 2500 m radial distance from the well (Δx) increases logarithmically until a maximum cell size of 100 m is obtained in 40 steps. This results in a total of ~40,000 cells for the model grid (with 60 m aquifer thickness). The cell size proved sufficiently small to provide converged results, with the maximum Courant number being 0.8 for all cells for the advection, which is sufficient to provide accurate simulations (Al-Maktoumi et al., 2007). Around the well, for the scenario where highest radial flow velocities are simulated, a maximum Peclet number of 1.95 occurs, calculated as the grid/mesh Peclet number proposed by Weatherill et al. (2004). The standard implicit finite difference solution is used with upstream weighting, with the PCG2 package used, with the groundwater flow solver and tolerance criteria set at 0.001. Other settings were tested which demonstrated negligible differences due to the relatively low Peclet number. To solve the heat flow equation, the Generalized Conjugate Gradient solver is used, with a tolerance of 10^{-9}.

To mimic the yearly variation in availability and demand of thermal energy, the yearly injection and extraction volumes are divided over the year following a sinusoidal curve (Fig. 3A). The peak injection and extraction represent the middle of winter and summer. Each simulated year consists of 1 month rest (no flow), 5 months injection, 1 month storage (no flow) and 5 months of extraction. Total injection and extraction volumes are equal, therefore resulting in volume balance. The total simulated operation time is 5 years for all simulations, after which a quasi-steady-state in thermal recovery efficiencies is achieved.

Fixed model parameters are shown in Table 1 and are based on previous studies and represent commonly found conditions in sandy aquifers and clayey aquitards.

2.3. Experimental design

The storage conditions within ATES systems of different injection temperatures were investigated. A structured sensitivity analysis was designed to see the effect of different parameter values on the modelling results. The varied storage conditions are the storage temperature (°C), aquifer thickness (m), horizontal and vertical hydraulic conductivity (m/d) and the yearly storage volume (m³), resulting in 180 unique simulations (Table 2). The range of geohydrological parameters represent values commonly found in sandy aquifers used for ATES (Bloemendal and Hartog, 2018; Sommer et al., 2013). Temperature and volume parameters are varied in relation to the expected size and temperature of ATES systems in practice (Kallesøe and Vangkilde-Pedersen, 2019). Next to this set of varied storage conditions, also some additional models were run that focused on specific features, e.g., for investigating variations in dispersion length, excluding advective in/outflow to assess conduction losses from a static cylinder or the tilting of a static thermal cylinder. The results from these models are shown in specific sections in the results and are described in more detail there. All simulation results that are presented in this study, unless stated otherwise, are dynamic
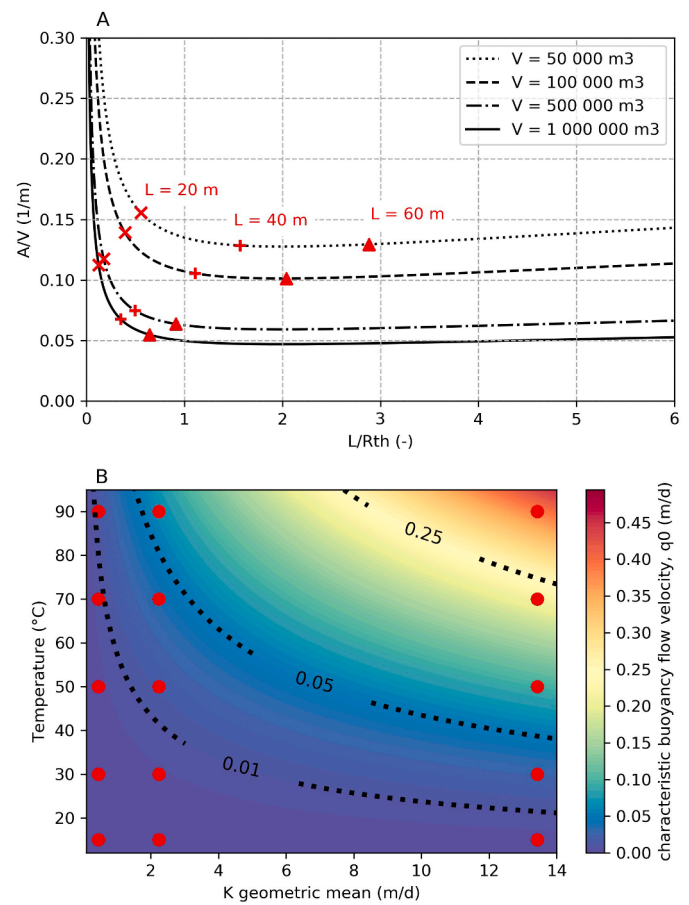

Fig. 4. A) The storage geometry parameters A/V (colors) and L/R_{th} (dotted lines) as function of the storage volume (m³) and the aquifer thickness (m). B) The characteristic buoyancy flow velocity q0 (m/d) as a function of the hydraulic conductivity geometric mean (x axis) and the storage temperature (y axis) calculated for an ambient (natural) groundwater temperature of 12 °C. The varying range of conditions that are simulated and analyzed in this study are indicated by the red marks in both A and B.

simulations following the injection-rest-extraction-rest flow pattern shown in Fig. 3.

The scenarios modelled in this study are presented against their respective storage geometry parameters (L/R_{th}) and (A/V) at the maximal injected volume in Fig. 4A, and for their modelled range of characteristic buoyancy flow velocity (q_0) in Fig. 4B.

2.4. Assessment framework

The simulated temperature extracted from the ATES well decreases during extraction. For each time step, the product of the average well temperature and the extracted volume results in the extracted amount of energy. The amount of energy that is not recovered after the yearly cycle is the amount of lost energy. Due to the energy losses, the sharp temperature front (that occurs during the first injection cycle) develops over the first few years into a transition front with a smooth temperature

Table 2
Model input parameters that are varied in the simulations, the <u>main dataset</u> assessed in this study.

Parameter	Symbol	Values	Unit
Storage temperature	T_{inj}	*1 5 | 30 | 50 | 70 | 90*	*°C*
Aquifer Thickness – Screen length	L_{aq}	*20 | 40 | 60*	*m*
Horizontal hydraulic conductivity aquifer at T = 12 °C	K_h	*1 | 5 | 30*	*m/d*
Yearly storage volume	*V*	*50 | 100 | 500 |1.000*	*$10^3 m^3$*

gradient. In addition, the aquitards above and below the storage aquifer are heated due to heat conduction. Hence, thermal losses are largest in the first few years. The simulations show that the 5th year thermal recovery efficiency is representative for the long term performance of ATES wells as energy losses stabilize relatively quickly after the first years. The fraction of energy that is recovered after storage is calculated as the thermal recovery efficiency (η) (Bloemendal and Hartog, 2018; Sommer et al., 2014):

$$\eta = \frac{E_{extracted}}{E_{injected}} = \frac{\int (T_{extracted} - T_{amb})Q_{extracted}C_w dt}{\int (T_{injected} - T_{amb})Q_{injected}C_w dt} = \frac{\overline{\Delta T}_{extracted}\overline{V}_{extracted}\overline{C}_w}{\overline{\Delta T}_{injected}\overline{V}_{injected}\overline{C}_w} \quad (9)$$

where $E_{extracted}$ and $E_{injected}$ is the total extracted and injected energy relative to the ambient groundwater temperature (*joule*), $T_{extracted}$ and $T_{injected}$ are the well temperatures during extraction and injection relatively, Q is the pumping rate (e.g. m³/day) and C_w is the volumetric heat capacity of water at 12 °C (4.18×10^6 J/m³/°C). Conversely to the yearly thermal recovery efficiency, the (annual) fraction of thermal energy losses, the loss fraction f_{loss} (-), is calculated as:

$$f_{loss} = 1 - \eta \quad (10)$$

3. Results

3.1. Thermal recovery efficiencies with increasing storage volume and temperatures

For the scenarios with injection temperatures of 15 °C and 30°C, results show that the thermal recovery efficiencies generally increase (the thermal loss fraction decreases) for increasing storage volumes (Fig. 5). Although the loss fractions (0.12–0.25) for the simulations for 30 °C storage temperatures are only slightly higher than their 15 °C counterparts, their variation within each volume class is notably higher. With increasing injection temperatures the variation increases further, with variation within each volume class being larger than the variation between the classes. With storage temperature <30 °C, the loss fraction

decreases from year 1 to year 5 between 0.09 and 0.14, while for the storage at 90 °C, the loss fraction increase is only between 0.03 and 0.14. For the worst performing scenarios at 90 °C storage temperature, more than 80 % of the stored energy is lost in the 1st year, only improving with 3 to 5 % in the next 4 years of operation. The loss fraction of the best performing scenarios at higher storage temperatures (50 – 90 °C), is similar to their 15 °C counterparts, illustrating that for certain conditions, the storage temperature does not impact the thermal recovery efficiency.

3.2. Thermal losses due to conduction

Fig. 6A shows the loss fraction against A/V for the scenarios at 15 and 30 °C. The linear relationship observed is an indication of losses being dominated by conduction (Bloemendal and Hartog, 2018). This same linear relationship is also observed as a lower limit for the large scatter in the relationship between A/V and loss fraction for the higher storage temperature scenario (50–90 °C, Fig. 6B). Apparently, for the high temperature scenarios that constitute this lower limit, conduction losses are still dominant. Still, also the A/V relationship observed for the low temperature scenarios, does come with some minor scatter (Fig. 6A), as was also observed in previous studies (Bloemendal and Hartog, 2018; Doughty et al., 1982; van Lopik et al., 2016). Therefore, to test the extent to which the origin of this scatter can still be related to conduction losses, the analytical expression by Doughty et al. (1982) for the recovery factor of a conductive static thermal cylinder (η^{cond}) was rewritten to express it as a function of A/V.

For a cylinder with given height (L) and thermal radius (R_{th}), situated in an isotropic homogeneous environment, the storage time (t, [days]) and the thermal diffusivity (D, [m²/day]), the recovery factor of a conductive static thermal cylinder is determined as (Doughty et al., 1982):

$$\eta^{cond} = \left(1 - 2\frac{\sqrt{Dt/\pi}}{R_{th}}\right)\left(1 - 2\frac{\sqrt{Dt/\pi}}{L}\right) \quad (11)$$
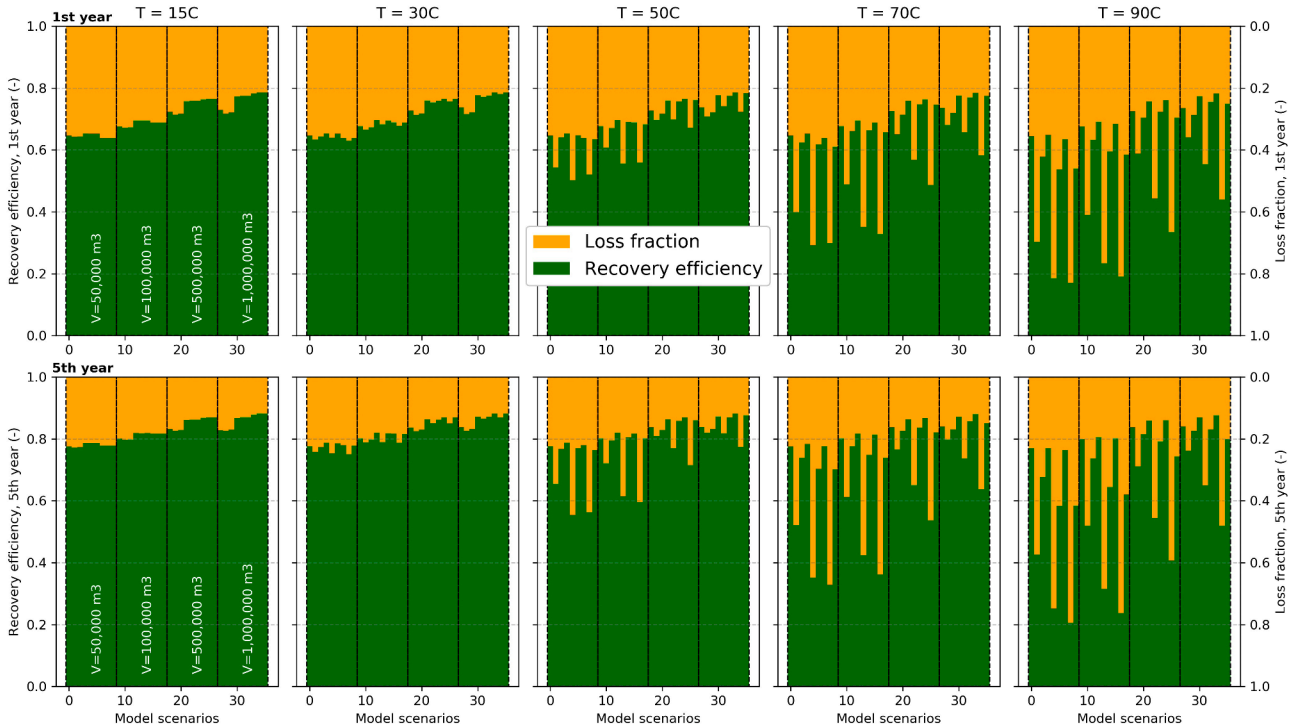

Fig. 5. The thermal recovery efficiency (green bars, left axis) and the thermal loss fraction (orange bars, right axis) for the 1st (above) and 5th (below) year of operation for the 36 different simulations performed for each storage temperature (15, 30, 50, 70 and 90 °C). The scenarios are ordered for increasing storage volume and are identical between all temperatures.
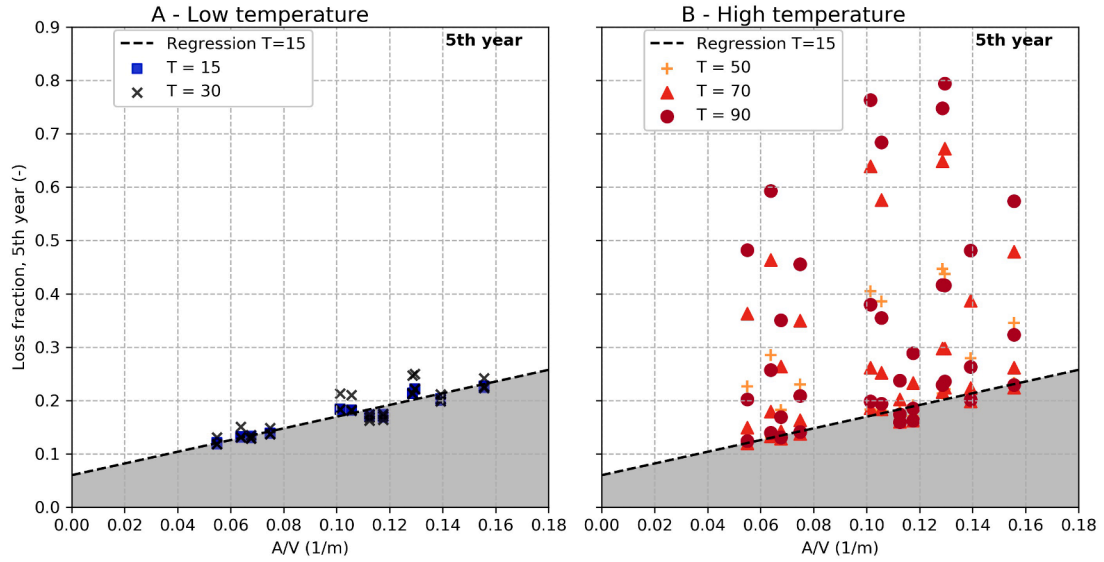
Fig. 6. Energy loss as a function of the A/V$_{th}$ ratio for the 5th year for all scenarios, sorted for A) low temperature (15 and 30 °C) and B) high temperature (50, 70, 90 °C). A representative minimal energy loss linear relationship with A/V is colored gray.

Here, the left term represents the radial factor (conduction into the aquifer) and the right term the vertical factor of heat conduction (conduction into the aquitards). The solution is valid when Dt/R_{th}^2 and Dt/L^2 $\ll 1$, which is the case for all scenarios in this study. As the ratio of A/V is equal to $2/L + 2/R_{th}$, rearranging gives the thermal recovery efficiency of a cooling cylinder as a function that includes A/V. With the loss fraction (f^{cond}) equal to 1-η (Eq. (10)), the loss fraction due to conduction from a static cylinder can be expressed as:

$$f_{loss}^{cond} = \sqrt{\frac{Dt}{\pi}}\left(\frac{A}{V}\right) - \frac{4Dt}{\pi R_{th}L} \qquad (12)$$

The resulting function (Eq. (12)) shows that the loss fraction due to conduction from a static cylinder is largely linearly related to the ratio of A/V multiplied by the square root term of storage time and thermal conductivity (Fig. 7). The right-hand term of the equation partly

compensates the loss of recovery efficiency for thermal cylinders with smaller radii and heights, and thus relatively large A/V (Fig. 7A), as the conduction losses into one direction are reduced by adjacent conduction losses when the cylinder is relatively small (small R_{th} and L). For the relevant storage conditions tested, the effect is however only limited (max 3 % at largest A/V) compared to the simplified linear A/V relationship (left term in Eq. (12)). The analytically calculated losses (red triangles in Fig. 7A) matched well with the numerically simulated cooling of a static thermal volume (no injection or abstraction, 330 days of cooling), tested for 4 storage geometries (A/V values) (black crosses in Fig. 7A).

When the injection and abstraction phases were included in the dynamic simulations (Fig. 7B), the numerical results agree best with the analytical solution (Eq. (12)) when the storage time (t) is 330 days, the maximum time that heat is stored in the aquifer (i.e. time between the beginning of injection to the end of extraction, see Fig. 1 for the
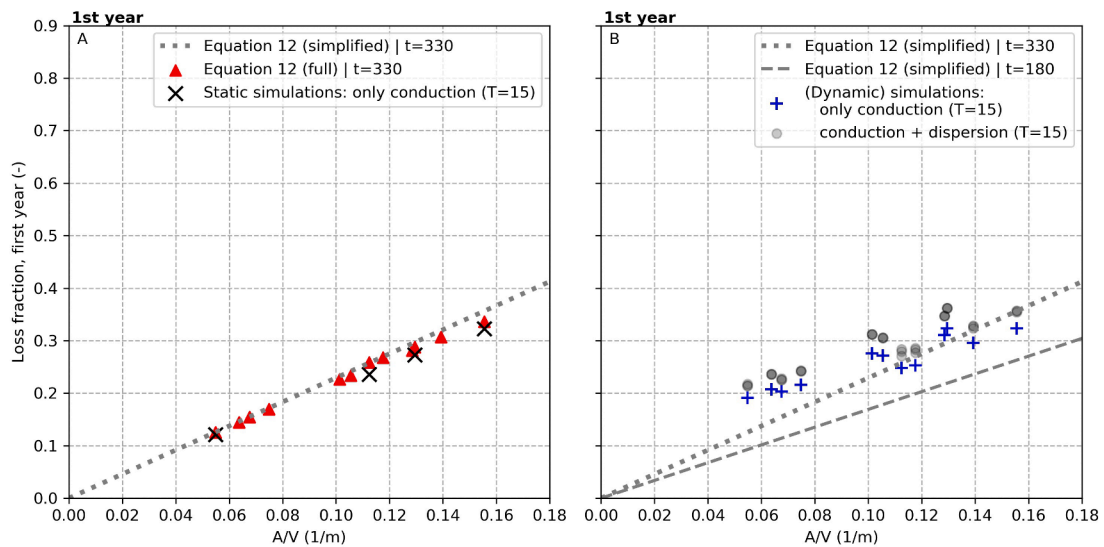

Fig. 7. A) The loss fraction for varying A/V for a cooling static cylinder ($t = 330$ days, $D = 0.053$). The line is the simplified relationship (Eq. (12)) with A/V and the full equation (red triangles) is used to calculate the results for the storage geometries varied in this study. These results are compared to 4 simulations of a static cylinder cooling for 330 days (black crosses). B) Dynamic simulations (including injection and abstraction phases) of the energy loss ratio after the first year of operation due to conduction only (blue crosses) and conduction with dispersion ($\alpha_l = 0.5$ m), compared to the simplified analytical linear relationship (Eq. (12)) of conductive cooling for $t = 330$ and $t = 180$ days storage time ($D = 0.053$).

injection/extraction protocol), rather than using the average storage time ($t = 180$ days) as observed in Fig. 7B. However, the simulated loss fraction of the dynamic ATES simulations deviate from the analytically derived results for 330 days storage, and appear elevated for the scenarios with the smallest A/V. Overall the analytical evaluation of losses due to conduction explains the strong relationship between A/V and thermal losses as found for the low temperature scenarios (Fig. 6A) and some of the high temperature scenarios (Fig. 6B), indicating conduction as the dominant processes for the thermal losses in these scenarios. Including dispersion ($\alpha_l = 0.5$ m, as included in the standard dataset, Fig. 6), in addition to conduction only simulations, leads to minor additional losses (2–3 %) while the A/V-f_{loss} correlation is maintained (Fig. 7B).

3.3. Thermal losses due to dispersion

Unlike conduction, mechanical dispersion losses only occur in the direction of flow at the thermal front into the aquifer (Fig. 2). This, in part, explains the only slight increase of total thermal losses when including dispersion ($\alpha_l = 0.5$ m) in addition to conduction (Fig. 7B). However, to evaluate the possible importance of dispersion losses at higher dispersivity values, additional ATES simulations were performed with $\alpha_l = 5$ m and compared to the analytical formulation of Tang and van der Zee (2021) for a 2D radial well system with a linear dispersion-velocity relationship, which is representative for the dispersion losses during the first year of ATES operation (Fig. 8, 1st year). The ratio of L/R_{th} gives the ratio of the surface area into the aquifer ($A_{aquifer}$) divided by the surface area into the aquitard ($A_{aquitard}$, Eq. (2)). With decreasing L/R_{th}, the losses due to dispersion decrease for a given storage volume as the relative area where dispersion losses occur (at the thermal front into the aquifer) decreases (Eq. (2)). The analytically calculated first year losses due to dispersion are relatively small (<13 %) when a dispersion length of $\alpha_l = 0.5$ m is applied (Fig. 8A). With a relatively large dispersion length of $\alpha_l = 5$ m, the losses are significantly higher for the storage conditions tested, particularly at larger L/R_{th} ratios (up to 38 % in the first year, Fig. 8B). As indicated by the difference between the analytical dispersion loss fraction and the dynamic simulations including both conduction and dispersion, conduction losses are dominant and account for more than 75 % of the total energy losses in the first year with $\alpha_l = 0.5$ m (Fig. 8A). At $\alpha_l = 5$ m, the importance of dispersion is about equal to the conduction process, especially at larger L/R_{th} ratio (Fig. 8B).

The observed loss fractions against L/R_{th} of the simulations in Fig. 8 for each storage volume is similar to the geometrical dependency of A/V with L/R_{th} shown in Fig. 4A. At L/R_{th} below 1, the ratio of A/V and hence conduction losses (Fig. 7), increase. While at L/R_{th} above 2 the loss fraction increases slightly due to increased conduction (slight increase of A/V at larger L/R_{th} in Fig. 4A) and dispersion losses (as indicated by the analytical increasing loss fraction of dispersion with L/R_{th} in Fig. 8). This is only observable for the two smallest storage volumes as the storage geometry of the larger storage volumes is smaller than $L/R_{th} = 2$ for the varied storage conditions. Nonetheless, Fig. 4A indicates that this would also occur due to conduction for the large storage volumes at higher L/R_{th}. Although the additional losses due to dispersion at $\alpha_l = 5$ is similar to conduction losses, the simulation results still show that at L/R_{th} below 0.5, heat loss increases (due to an increase of A/V, Fig. 7). The results thus indicate that the increase of conduction losses at small L/R_{th} is more dominant than the decrease of dispersion losses, even at relatively large values of dispersion length ($\alpha_l = 5$ m, Fig. 8B).

3.4. Thermal losses due to buoyancy-driven flow

With the increase of buoyancy-driven flow at higher temperatures, and the only limited impact of dispersion on the thermal losses in the main dataset ($\alpha_l = 0.5$), the large additional losses relative to the A/V relationship for the high temperature scenarios in Fig. 6B are due the
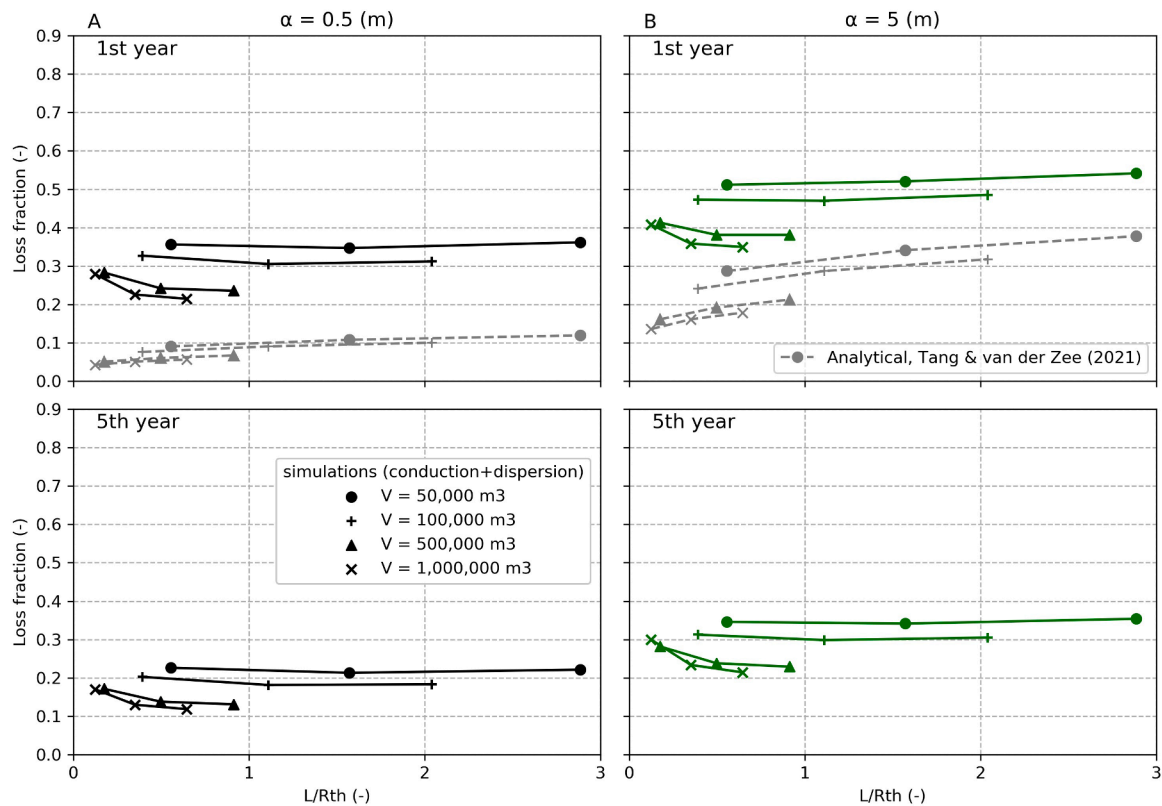

Fig. 8. Simulated ($T = 15\ ^\circ$C, including conduction and dispersion) 1st year (top) and 5th year (bottom) energy losses for A) the standard dataset ($\alpha_l = 0.5$ m) and B) for $\alpha_l = 5$ m. The dispersion only analytically calculated loss fraction is also shown for both $\alpha_l = 0.5$ m and $\alpha_l = 5$ m in the 1st year.
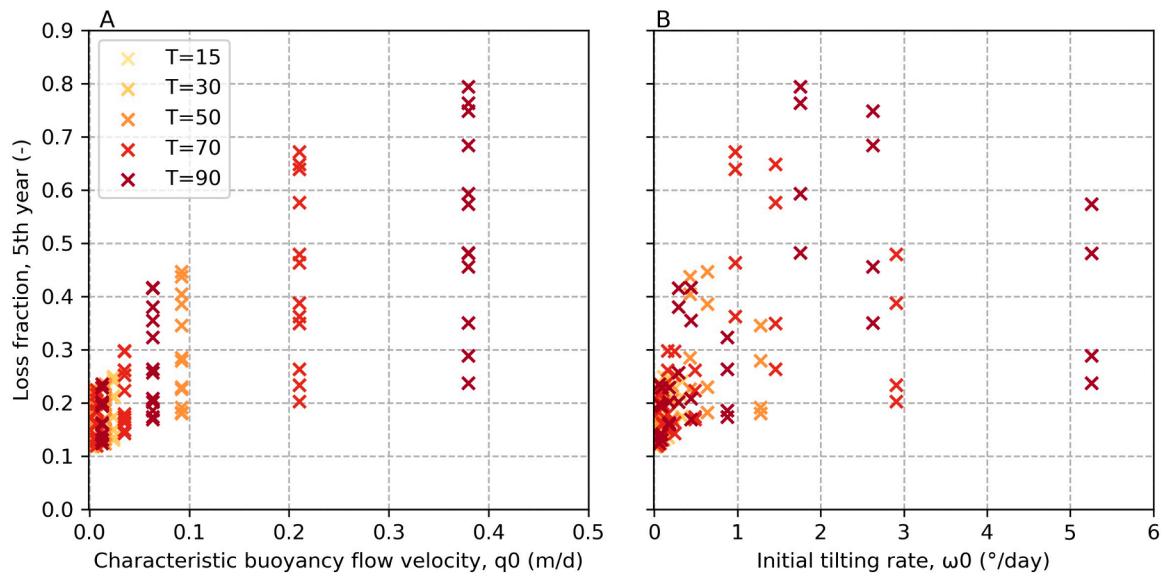
Fig. 9. Loss fraction in the 5th year as a function of the characteristic buoyancy flow velocity q_0 (A) and the initial tilting rate ω_0 (B) for the total standard dataset.

impact of buoyancy-driven flow. This is illustrated by the general increase in total thermal loss fraction (Fig. 9A) with the increase of characteristic buoyancy flow velocity (q_0, Eq. (5)). The low and limited range in the total loss fraction in the 5th year (0.12–0.24) for the lowest values of the characteristic buoyancy flow velocity, are attributed to conduction and dispersion only. With increasing values of q_0 (>0.05 m/d), the range in the thermal loss fraction is increasing, with the highest loss fraction range (0.22 – 0.8) for the highest q_0 (0.38 m/d). The initial tilting rate of the thermal front (ω_0, Eq. (6)), which also takes into account varying aquifer thicknesses, does not correlate for all scenarios with the total thermal loss fraction (Fig. 9B). Although the maximal loss fraction increases for larger ω_0, similarly to q_0, the correlation between ω_0 and the loss fraction is still poor.

3.4.1. Geometric analysis of the effect of tilting

To evaluate to what extent the limited correlation of the initial tilting rate (Fig. 9) with the observed loss fraction is due to a dependency on the geometry of the thermal storage volume, the amount of volume that is displaced for certain tilting angles was calculated for varying storage geometries (varying aquifer thickness and storage volume). Assuming that the tilting angle is constant over the full height of the aquifer, the volume that is lost for a particular tilting angle is calculated using the volume of a conical frustum, i.e. a tilted cylinder (Fig. 10A):

$$V_{conical,frustum} = \frac{1}{3}\pi L \left(R_{bottom}^2 + R_{top}^2 + R_{bottom}R_{top} \right) \quad (13)$$

where R_{top} is the thermal radius at the top of the aquifer and R_{bottom} is the radius at the bottom. For a tilted thermal volume, the volume that is lost beyond recovery is subsequently calculated as the amount of volume that reaches beyond the thermal front as a result of tilting (Fig. 10A):

$$V_{loss} = \frac{1}{3}\pi \frac{L}{2} \left(R_{th}^2 + R_{th\_buoyancy}^2 + R_{th}R_{th\_buoyancy} \right) - \pi \frac{L}{2}R_{th}^2 \quad (14)$$

By dividing this volume by the stored volume, and rearranging, the loss fraction due to tilting is written as a function of the tilting angle β (rad) and the ratio of the aquifer thickness divided by the thermal radius (L/R_{th}):

$$f_{loss}^{tilting} = \frac{\tan(\beta)^2}{24}\left(\frac{L}{R_{th}}\right)^2 + \frac{\tan(\beta)}{4}\left(\frac{L}{R_{th}}\right) \quad (15)$$

On the basis of this geometrical evaluation it is thus expected that the loss fraction increases near linearly with increasing L/R_{th} for a particular tilting angle of the thermal front as it is being abstracted (Fig. 10B).

This strong dependency of the thermal loss fraction on L/R_{th} is also reflected by the results of 3 types of numerical simulations with equal
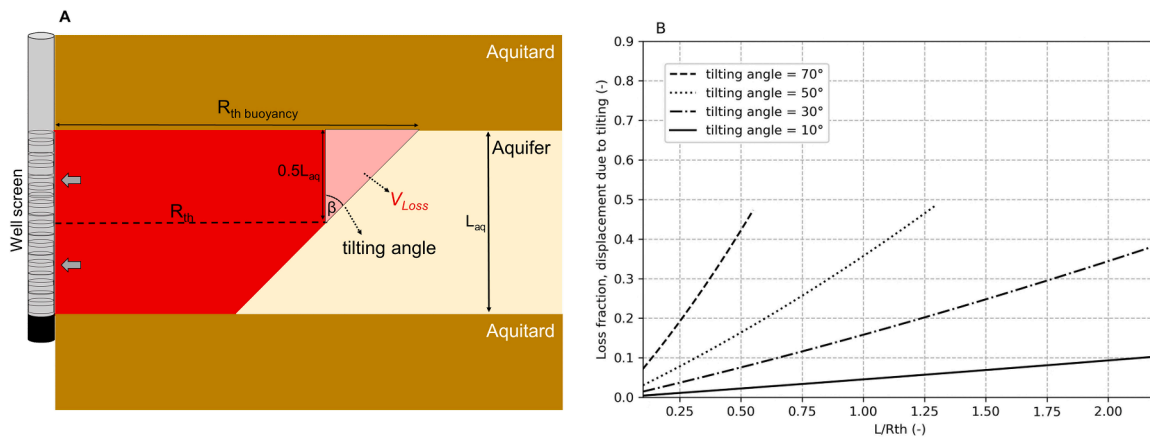

Fig. 10. A) Conceptual representation of the geometry of a tilted thermal volume with a linear tilting front of tilting angle (β) in an aquifer with thickness L (m). B) The geometrically calculated loss fraction due to displacement as a function of L/R_{th} for 4 constant tilting angles.
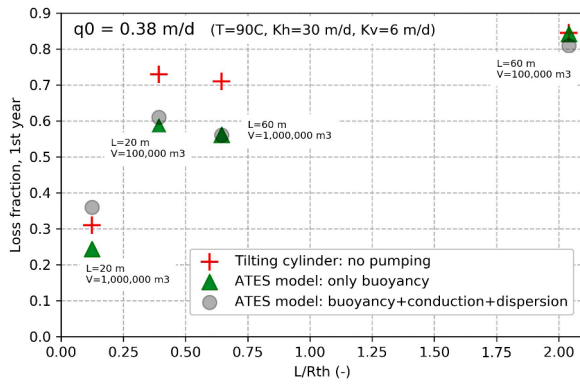
Fig. 11. Loss fraction versus L/R_{th} for 90 °C storage temperatures in a highly permeable aquifer ($K_h = 30$, $K_v = 6$ m/d) using 3 simulation setups: 1) A tilting cylinder without any pumping (330 days of tilting). 2) an ATES model that only includes buoyancy-driven flow. And 3) the normal ATES model that includes conduction, dispersion and buoyancy-driven flow. The specific storage conditions (L (m) and V (m³)) of each scenario are given in the plot.

storage conditions for four varying storage geometries shown in Fig. 11. Firstly, the tilting of a static thermal volume (no injection or abstraction) (red plus in Fig. 11). Secondly, the tilting of a thermal volume for an dynamic ATES simulation including the forced convection injection and abstraction phase (only considering buoyancy-driven flow but not dispersion and conduction) (green triangle in Fig. 11). Thirdly, the normal dynamic simulation that includes the dynamic simulation including buoyancy-driven flow, conduction and dispersion (gray circle in Fig. 11). The behavior of the static tilting cylinder is comparable to the results of the dynamic ATES simulations. However, for the two middle scenarios at L/R_{th}, =0.4 and 0.6, the losses of the ATES models are 0.1-0.12 lower. Hence, the effect of the radial advective flow from the wells is limited, but has a small positive impact on the effects of buoyancy-driven flow for these scenarios. When conduction and dispersion are included, the simulation that is strongly impacted by the tilting effect (at highest L/R_{th}) has relatively lower thermal loss because the mixing zone that is created by these processes decreases the tilting effect. Oppositely for low L/R_{th}, the tilting effect is relatively small and conduction and dispersion lead to increased thermal losses.

3.4.2. Effect of hydraulic conductivity anisotropy

When tilting occurs, groundwater flows in both a vertical (upward) and horizontal direction (away from the well at the top and towards the well at the bottom). The geometric mean is often used to average the hydraulic conductivity of the aquifer in both directions, as is the case for
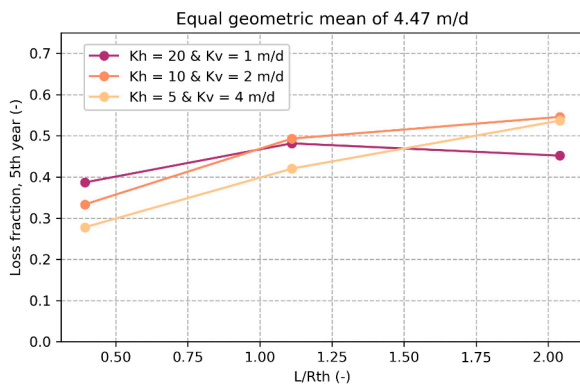

Fig. 12. Loss fraction versus L/R_{th} for additional simulations with equal geometrically averaged $K = 4.47$, but for varying anisotropy (K_h /K_v). The storage temperature is 90 °C, total storage volume is 100,000 m³ and the aquifer thickness is varied between 20, 40 or 60 m.

the characteristic buoyancy flow velocity (Eq. (12)) and initial tilting rate (Eq. (13)). However, the same geometric mean can be obtained by using different anisotropy factors (γ_{ani}). For the same geometric mean, varying anisotropy leads to different thermal losses for varying storage geometries (Fig. 12). Equal to the results of the standard dataset where $\gamma_{ani} = 5$, the impact of buoyancy-driven flow decreases with smaller L/R_{th} for the two scenarios with the smallest anisotropy ($\gamma_{ani} = 1.25$ & 5). Here, lower K_h seems to limit for buoyancy-driven flow to occur, as the results of the 5/4 (K_h/K_v) scenario have lower losses than the 10/2 scenario. For the scenario with high K_h and low K_v (20/1), lower vertical hydraulic conductivities limit the tilting flow and the loss fraction decreases moderately for the largest L/R_{th}. In these cases, most of the flow needs to go vertically, and therefore, tilting is reduced strongest for the storage geometries that are vertical flow dominated (large L/R_{th}). For these scenarios with very high anisotropy, the overall effect of reduced tilting on the thermal recovery efficiency is positive, even though high L/R_{th} geometry itself is geometrically disadvantageous when tilting occurs (Fig. 10). Hence, for low L/R_{th}, the horizontal component of the hydraulic conductivity is most important and for large L/R_{th} the vertical component is most critical.

3.5. Net effect of interacting processes and storage geometry

Thermal losses due to conduction and dispersion occur for any ATES system, and depending on the used longitudinal dispersion length of the aquifer the thermal losses could be dominated by conduction or be the net effect of both conduction and dispersion (Fig. 8). At limited potential for buoyancy-driven flow ($q_0 = 0.013$ m/d in Fig. 13), conduction is the most dominant process leading to heat losses in the standard dataset, and the loss fraction increases when the ratio of A/V increases at increasingly smaller L/R_{th} below 1 (Fig. 4A). Depending on the storage temperature and the hydraulic conductivity of the aquifer, the potential for buoyancy-driven flow becomes significant at $q_0 > 0.05$ m/d (Fig. 13). When moderate potential for buoyancy-driven flow exists, at $q_0 = 0.092$ in Fig. 13, the effects of increased losses due to buoyancy-driven flow are observed as more additional heat losses are observed at larger L/R_{th} for each storage volume group, especially in year 5. Hence, as the heat losses decrease with decreasing L/R_{th} for systems with high impact of buoyancy-driven flow, conditions that are not most suitable for conduction losses (small L/R_{th}) are considered increasingly more suitable for these systems at higher q_0 (Fig. 11, Fig. 13). For the most buoyant scenario ($q_0 = 0.38$ m/d), low L/R_{th} storage geometry (<0.5) is essential to mitigate the potential effect of buoyancy-driven flow (0.8 – 0.4 loss fraction difference in 5th year where $L/R_{th} > 0.5$), indicating that buoyancy-driven flow is under these conditions the most dominant process leading to heat losses. In time (1st versus 5th year), the performance of ATES wells increases about 50 % when conduction and dispersion are the dominant process ($q_0 = 0.013$ m/d, Fig. 13). For scenarios experiencing strong heat losses due to tilting at q_0=0.38 m/d and relatively large L/R_{th}, the loss fraction only decreases up to 2 % in 5 year time. Hence, when an ATES well that is prone to buoyancy-driven flow (at high q_0) is operated at unsuitable storage conditions (high L/R_{th}), the thermal recovery efficiency tends to stay low during operation.

4. Discussion

4.1. Near-linear relationship of thermal conduction loss fraction with A/V

The near-linear analytical relationship between the thermal area over volume ratio (A/V) and the thermal loss fraction, due to conduction from a static thermal cylinder (Eq. (12)) as derived in this study, supports the linear correlation observed in numerical simulations in this and previous ATES studies (Bloemendal and Hartog, 2018; Doughty et al., 1982; van Lopik et al., 2016). However, the lack of full linearity in the analytical formulation only partly explains the scatter observed for simulated conduction losses of ATES for the first year (Figs. 6A, 7B).
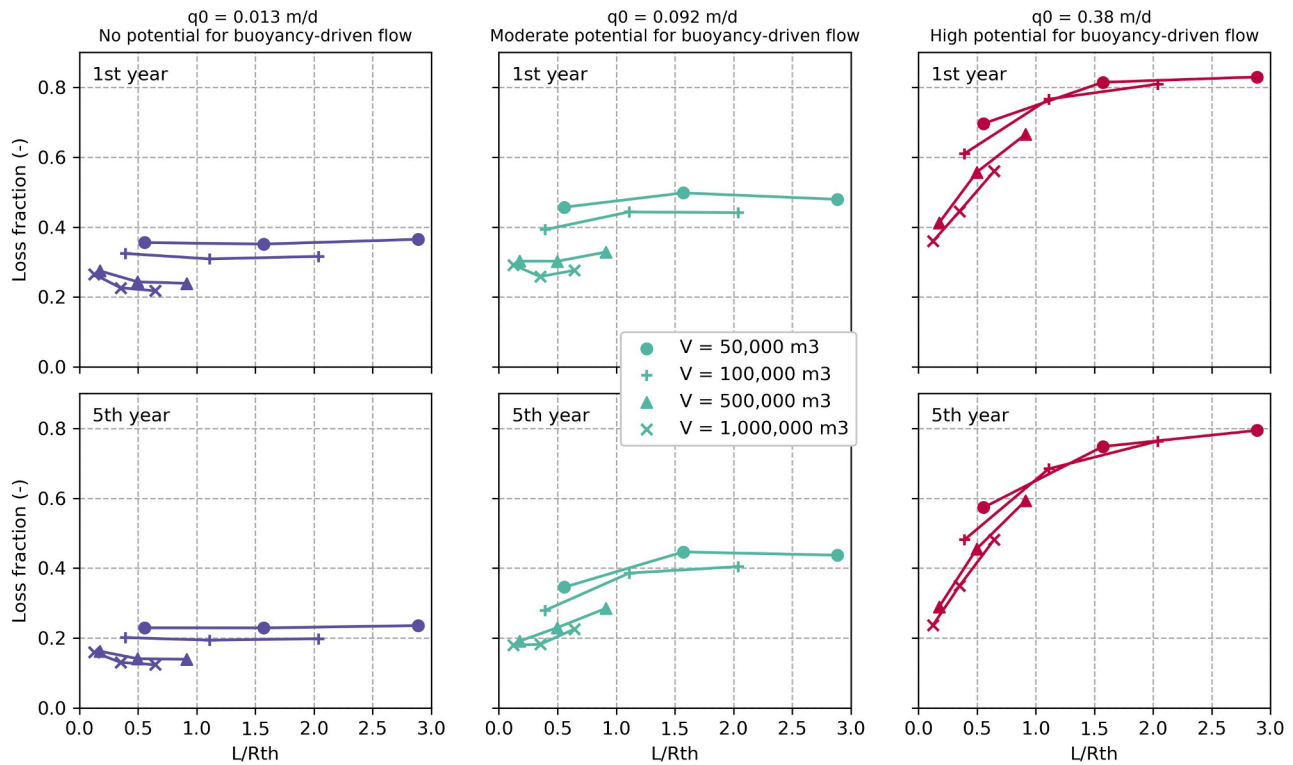
Fig. 13. Loss fraction for three equal q_0 sets of ATES scenarios (left – right increasing q0) as a function of the storage geometry L/R$_{th}$. All scenarios are at 90 °C storage temperature, but the hydraulic conductivity (K$_h$|K$_v$) varies from left: 1|0.2 – 5|1 – 30|6 m/d. The lines indicate scenarios of equal storage volume.

Unlike in the analytical relationship, the simulated thermal losses, in this and the above mentioned studies, do not approach zero thermal loss fraction with a small A/V (Fig. 7B). As this occurs when the actual injection – storage – extraction cycle is modelled, and not when a static thermal cylinder is modelled (or calculated analytically) (Fig. 7A), these increased conduction losses occur due to the moving (expanding or decreasing) thermal volume shape. Next to the variation in observed scatter, the angle and position of the linear correlation line varies between the simulations results of this and previous studies (Fig. 13 in Bloemendal and Hartog (2018)). As the thermal conductivity (κ_{aq}) (from 2 to 2.55) and injection-storage-extraction regimes (sinusoidal distribution versus block distribution) vary between all of the above mentioned studies, a varying slope of the linear correlation line is indeed expected according to the dependency of conduction losses on the square root of the product of κ_{aq} and t in Eq. (12). Although the analytical formulation (Eq. (12)) does not describe the simulated thermal loss fraction exactly, it provides a simple analytical basis to assess the expected effects of conduction for varying storage geometry and storage conditions (t, κ_{aq}),

4.2. The relative role of mechanical dispersion

For the conditions tested in this study, mechanical dispersion leads to relatively small additional thermal loss fraction compared to conduction, especially at $\alpha_l = 0.5$ m (Fig. 8). This is related to the fact that mechanical dispersion only leads to additional mixing when there is advective movement of the groundwater during injection and extraction and not when the well is idle (Gelhar and Collins, 1971). Moreover, it occurs only radially at the thermal front, while conduction occurs both into the aquifer (simultaneously with dispersion) and into the aquitard. Logically, when relatively large values of longitudinal dispersion lengths are used in simulations studies, dispersion has a strong impact. With $\alpha_l = 5$ in this study, $\alpha_l = 10$ m in Sheldon et al. (2021) or even up to $\alpha_l = 100$ m in Gao et al. (2019)), dispersion losses are equal or sometimes

even larger than the losses due to conduction. Large values of α_l are indeed reported in literature (Gelhar et al., 1992; Zech et al., 2022) for the length-scale of realistic thermal radii (Sheldon et al., 2021) for ATES systems ($R_{th} = 50 – 150$ m). However, large values of α_l like these seem to overestimate the actual effect of additional mixing due to macrodispersion for ATES systems (Sommer et al., 2013). In their study, it is shown that only for highly heterogeneous conditions (log hydraulic conductivity std. dev. >1), the effect of additional mixing due to hydraulic conductivity heterogeneity (macrodispersion) is represented by longitudinal dispersion lengths larger than 1 m, up to about a maximum of 5 m. Reasons for these relatively small longitudinal dispersion lengths are that heat transport occurs slower due to thermal retardation due to heat adsorption by the solid aquifer material (Bloemendal and Hartog, 2018), ATES systems are cyclic and thus preferential flow paths are again used during extraction and thereby limiting its effect and because conduction dampens (spreads vertically) the effect of horizontal/radial extrusions in preferential flow paths that occur due to heterogeneity (Ferguson and Woodbury, 2007; Sommer et al., 2013). Hence, for the range of dispersion lengths that represent additional mixing in ATES systems for a realistic range of heterogeneity of sedimentary aquifers, a limited impact of dispersion is expected.

4.3. The relative impact of buoyancy-driven flow depends on storage geometry

Many of the previous studies on ATES studied the role of buoyancy-driven flow on heat losses at high storage temperatures (>60 °C, e.g. Gao et al. (2019); van Lopik et al. (2016)). Consequently, the conditions considered were relatively susceptible to the occurrence of buoyancy-driven flow (e.g. relatively small storage volumes of 10,000 – 100,000 m³/year). However, as shown by the wider range of realistic conditions tested in this study, the impact of buoyancy-driven flow can vary from insignificant (<1 % of total losses) even at the highest storage temperatures tested (90 °C) to strongly dominating (>80 % of total

losses). In addition to conditions that reduce the potential for buoyancy-driven flow (e.g. lower storage temperatures, lower hydraulic conductivities), this study highlights that larger storage volumes and favorable storage geometries may even prevent strong buoyancy-driven flow from having a significant impact (Fig. 13), when the tilting of the thermal front in the aquifer occurs relatively far from the injection well (at low L/R_{th}). Although the geometrical derivation (Eq. (15)) of the thermal loss fraction for a given tilting angle illustrates this strong geometrical dependency (Fig. 10), this formula is not simply used to estimate the loss fraction of a specific ATES system due to buoyancy-driven flow as the tilting angle that occurs for an ATES system is not static and cannot be determined analytically as it is influenced by the width of the thermal front zone (Doughty et al., 1982), which increases with each year due to conduction and dispersion, and due to advective movement from the well during injection and extraction (Hellström et al., 1988b).

4.4. The importance of uncertainty in thermal and hydraulic properties for ATES performance

Typically, for the application of ATES in practice, there is considerable uncertainty in the subsurface parameters that may affect the thermal recovery efficiency (e.g. thermal conductivity, hydraulic conductivity). Since the different processes that lead to thermal losses depend on different parameters, the potential impact of parameter uncertainty depends on the importance of the heat loss processes that depend on it.

As the impact of dispersion is relatively small for the range of expected representative longitudinal dispersion lengths for ATES systems, the importance of unknown or uncertain longitudinal dispersion length is expected to be relatively limited in practice. At low storage temperatures, thermal conduction is therefore in general the dominant process for thermal losses of ATES, which is related directly to the thermal conductivity (Eq. (12)) as other sedimentological and thermal properties like the volumetric heat capacity and porosity do not significantly affect conduction losses (Doughty et al., 1982; Rau et al., 2012; Schout et al., 2014). The range of thermal conductivity of unconsolidated sands (κ_s) and clays (κ_c) reported in literature are maximally between 1 – 3 and 1.1 – 3.1 W/m/K, respectively (Dalla Santa et al., 2020), with the average being ~2 for both properties (equal values are used in this study ($\kappa_s = \kappa_c = \kappa_{aq} = 2$). When comparing the thermal loss fraction that occurs for the minimum ($\kappa_{aq} = 1$), average ($\kappa_{aq} = 2$) and maximum ($\kappa_{aq} = 3$) thermal conductivity for the range of realistic storage geometries (A/V) assessed in this study, calculated with the analytical solution (Eq. (12)) using the same porosity and heat capacities assumed in this study (Table 1), the thermal loss fraction varies from 10 to 14 to 17 % in the first year for the smallest A/V ratio. For the scenario with highest A/V, where conduction leads to strong thermal losses for $\kappa_{aq} = 2$ (41 % 1st year), the variation in thermal conductivity has a much stronger effect with the thermal loss fraction ranging from 30 to 41 to 50 %. While this indicates that the thermal conductivity indeed is of importance, low A/V value ensures that the impact of thermal conductivity on the overall performance of the ATES systems remains low, even for relatively high values of κ_{aq}.

The impact of buoyancy-driven flow starts to become significant at $q_0 > 0.05$ m/d, at relatively high storage temperature, for high hydraulic conductivity of the aquifer, or both (Fig. 4A). As the horizontal hydraulic conductivity (K_h) may strongly vary in practice for semi-unconsolidated aquifers (e.g. between 1 and 30 m/d based on ATES in the Netherlands (Bloemendal and Hartog, 2018)) and the potential for buoyancy-driven flow (q_0), and thus its potential impact, varies strongly for this range of hydraulic conductivities (assuming $\gamma_{ani} = 5$ in Fig. 4A), a large range of uncertainty of ATES performance is associated with the uncertainty of hydraulic conductivity. Especially for conditions when the potential impact of buoyancy-driven flow is high (due to high q_0 or unfavorable, relatively high, L/R_{th}), detailed knowledge of K_h and especially K_v (Fig. 13) must be obtained. Although K_h is already quite variable and

typically uncertain, the representative anisotropy of a medium, is even harder to determine in practice (Maier et al., 2022), and therefore adds another degree of uncertainty. When layers of lower hydraulic conductivity are present in aquifers, which strongly decreases the potential for buoyancy-driven flow (Doughty et al., 1982), the hydraulic conductivity could be represented with relatively large anisotropy factors of e.g. 20 – 100 (Burger and Belitz, 1997; Huysmans and Dassargues, 2005), compared to reported anisotropy factors (3 – 10) for relatively homogeneous sands (Lake, 1988; Xynogalou, 2015). Hence in practice, when only the horizontal (aquifer scale) hydraulic conductivity is measured, the potential impact of buoyancy-driven flow is still uncertain as the representative K_v is still highly uncertain (Beernink et al., 2022).

4.5. Implications for assessing ATES performance in practice

Despite the range of different factors and parameters that affect the different thermal loss processes, the storage geometry parameters A/V and L/R_{th} proved to be useful to assess and improve the expected thermal performance of ATES systems in this study. Three example ATES systems having different storage geometries are shown in Fig. 14. When there is only limited potential for buoyancy-driven flow (at low q_0) for the ATES thermal volume with storage geometry of $L/R_{th} = 0.5$ in Fig. 14, the cylindrical storage volume (indicated by the black striped line) would have a relatively large A/V value as L/R_{th} is larger than 2 (A/V is minimal when the aquifer thickness is equal to the diameter of the stored volume at $L/R_{th} = 2$ (Fig. 4A)) being sub-optimal for heat losses due to conduction (Fig. 8). In contrast however, the impact of dispersion decreases with L/R_{th} and particularly for ATES systems with a high potential for buoyancy-driven flow ($q_0 > 0.05$ m/d, red areas in Fig. 14), increasingly smaller L/R_{th} ratios (<1) strongly reduce the heat losses due to tilting. The ATES system with storage geometry of $L/R_{th} = 2$ in Fig. 14 would be most suitable for a conduction dominated system, while a storage geometry of $L/R_{th} = 0.5$ the (tilted) thermal front is far away from the well screen, which would be more efficient to reduce heat losses due to dispersion and especially buoyancy-driven flow.

Hence, in practice it is important to assess if a strong potential for buoyancy-driven flow is anticipated due to high temperature and/or high hydraulic conductivity (based on e.g. q_0). If so, a relatively thin aquifer could be aimed for resulting in small L/R_{th}. Similarly, when multiple aquifers are available with equal aquifer thickness, the aquifer with relatively low representative hydraulic conductivity could be used to reduce the potential of buoyancy-driven flow to occur. However, these design choices also have implications for e.g. maximal storage volume per ATES well, which is mainly determined by the hydraulic conductivity of the aquifer and the total screen length that is being installed (van Beek et al., 2009). When changes aimed to minimize the impact of buoyancy-driven flow or conduction lead to the need for extra wells, this could have a major impact on the CAPEX of the system (Bloemendal et al., 2020; Daniilidis et al., 2022; van der Roest et al., 2021). Moreover, also the prevention of well clogging, mutual interaction and the cost of drilling and installation play a role (Bloemendal and Hartog, 2018; Houben, 2015) when choosing a suitable storage aquifer. Hence, a broad analysis is needed in practice to assess the specific suitability of aquifers and ATES design.

5. Conclusions

In this study, the heat losses of stored thermal volumes of ATES systems were investigated to determine what the relative contribution of dispersion, conduction and buoyancy-driven flow is to ATES heat losses under various storage conditions and how ATES design is improved accordingly. The numerical and analytical results in this paper confirm previous research that the ratio of the well screen length (aquifer thickness) divided by the thermal radius (L/R_{th}) and the ratio of the stored thermal surface area to the storage thermal volume (A/V) are
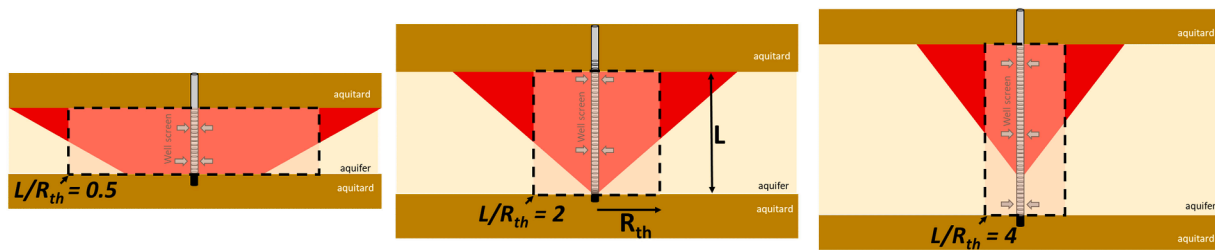
Fig. 14. Schematic overview of the potential storage geometry of storing equal thermal volumes in a thin (left, L/R$_{th}$ = 0.5), medium (middle, L/R$_{th}$ = 2) and thick (right, L/R$_{th}$ = 4) aquifer for a situation without tilting (striped edge) and with tilting due to buoyancy-driven flow (red space).

useful parameters to assess and improve the storage geometry.

With respect to thermal losses due to dispersion and conduction, it was shown that for the expected range of storage conditions of ATES systems in practice, conduction generally dominates over the effect of macrodispersion. Heat losses due to conduction are minimized at small A/V, with A/V, for a given storage volume, being minimized at $L/R_{th} = 2$. Next to this, the impact of dispersion is minimized for decreasing L/R_{th} as calculated analytically. However, the simulation results of this study show that at low L/R_{th} (<1), conduction again leads to an increase of heat losses as the ratio of A/V increases for small L/R_{th}.

The wide range of realistic conditions tested in this study show that the impact of buoyancy-driven flow varies strongly, and even for storage temperatures of 90 °C, ranges from insignificant (<1 % of total losses) to strongly dominating the overall heat losses (>80 % of total losses). In addition to conditions that reduce the potential for buoyancy-driven flow (e.g. lower storage temperatures, lower hydraulic conductivities), this study shows that the impact of buoyancy-driven flow is decreased when the L/R_{th} is small ($L/R_{th} < 1$), i.e. the thermal front is situated relatively far away from the well.

From these observations, it follows that for the storage geometry a relatively small value of L/R_{th} (<1) is not preferred when conduction dominates the heat losses. However on the contrary, for the potential impact of dispersion and especially buoyancy-driven flow at $q_0 > 0.05$ m, small L/R_{th} is preferred. Hence, in practice this means that the suitability of aquifers (thickness, hydraulic conductivity) is determined by the operational boundary conditions (storage volume, storage temperature, required flow rate). The introduced practical measures and description in this study are useful to straightforwardly asses feasibility and optimize the initial design of ATES systems prior to complex modelling efforts.

CRediT authorship contribution statement

Stijn Beernink: Conceptualization, Methodology, Software, Visualization, Validation, Formal analysis, Investigation, Writing – original draft, Writing – review & editing. **Niels Hartog:** Conceptualization, Methodology, Investigation, Writing – review & editing, Supervision, Funding acquisition. **Philip J. Vardon:** Methodology, Writing – review & editing, Supervision, Funding acquisition. **Martin Bloemendal:** Conceptualization, Methodology, Software, Writing – review & editing, Supervision, Funding acquisition.

Declaration of Competing Interest

The authors declare that they have no known competing financial interests or personal relationships that could have appeared to influence the work reported in this paper.

Data availability

Data will be made available on request.

References

Al-Maktoumi, A., Lockington, D.A., Volker, R.E., 2007. SEAWAT 2000: modelling unstable flow and sensitivity to discretization levels and numerical schemes. Hydrogeol. J. 15 (6), 1119–1129. https://doi.org/10.1007/s10040-007-0164-2.

Anderson, M.P., 2005. Heat as a ground water tracer. Groundwater 43 (6), 951–968. https://doi.org/10.1111/j.1745-6584.2005.00052.x.

Bakker, M., Post, V., Langevin, C.D., Hughes, J.D., White, J.T., Starn, J.J., Fienen, M.N., 2016. Scripting MODFLOW model development using Python and FloPy. Groundwater 54 (5), 733–739. https://doi.org/10.1111/gwat.12413.

Beernink, S., Barnhoorn, A., Vardon, P.J., Bloemendal, M., Hartog, N., 2022. Impact of vertical layering and the uncertainty and anisotropy of hydraulic conductivity on HT-ATES performance. In: Paper presented at the European Geothermal Congress 2022. Berlin.

Bloemendal, M., Hartog, N., 2018. Analysis of the impact of storage conditions on the thermal recovery efficiency of low-temperature ATES systems. Geothermics 17, 306–319. https://doi.org/10.1016/j.geothermics.2017.10.009.

Bloemendal, M., Vardon, P.J., Medema, A., Snelleman, S., Marif, K., Beernink, S., . . . Van Oort, T. (2020). *Feasibility study HT-ATES at the TU Delft campus*. Retrieved from https://www.warmingup.info/documenten/window-fase-1-a1-verkenning-hto-tud-feasibilityht_ates_tudelft.pdf.

Burger, R.L., Belitz, K., 1997. Measurement of anisotropic hydraulic conductivity in unconsolidated sands: a case study from a shoreface deposit, Oyster, Virginia. Water Resour. Res. 33 (6), 1515–1522. https://doi.org/10.1029/97WR00570.

Buscheck, T.A., Doughty, C., Tsang, C.F., 1983. Prediction and analysis of a field experiment on a multilayered aquifer thermal energy storage system with strong buoyancy flow. Water Resour. Res. 19 (5), 1307–1315. https://doi.org/10.1029/WR019i005p01307.

Caljé, R., 2010. MSc. Delft University of Technology, Delft.

Dalla Santa, G., Galgaro, A., Sassi, R., Cultrera, M., Scotton, P., Mueller, J., Bernardi, A., 2020. An updated ground thermal properties database for GSHP applications. Geothermics 85, 1–13. https://doi.org/10.1016/j.geothermics.2019.101758.

Daniilidis, A., Mindel, J.E., De Oliveira Filho, F., Guglielmetti, L., 2022. Techno-economic assessment and operational CO$_2$ emissions of High-Temperature Aquifer Thermal Energy Storage (HT-ATES) using demand-driven and subsurface-constrained dimensioning. Energy 249, 1–17. https://doi.org/10.1016/j.energy.2022.123682.

Dincer, I., 2002. Thermal energy storage systems as a key technology in energy conservation. Int. J. Energy Res. 26 (7), 567–588. https://doi.org/10.1002/er.805.

Doughty, C., Hellström, G., Fu Tsang, C., 1982. A dimensionless parameter approach to the thermal behavior of an aquifer thermal energy storage system. Water Resour. Res. 18 (3), 571–578. https://doi.org/10.1029/WR018i003p00571.

Ferguson, G., Woodbury, A.D., 2007. Urban heat island in the subsurface. Geophys. Res. Lett. 34 (23), 1–4. https://doi.org/10.1029/2007 gl032324.

Fleuchaus, P., Godschalk, B., Stober, I., Blum, P., 2018. Worldwide application of aquifer thermal energy storage – a review. Renew. Sustain. Energy Rev. 94, 861–876. https://doi.org/10.1016/j.rser.2018.06.057.

Gao, L., Zhao, J., An, Q., Liu, X., Du, Y., 2019. Thermal performance of medium-to-high-temperature aquifer thermal energy storage systems. Appl. Therm. Eng. 146, 898–909. https://doi.org/10.1016/j.applthermaleng.2018.09.104.

Gelhar, L., Collins, M., 1971. General analysis of longitudinal dispersion in nonuniform flow. Water Resour. Res. 7 (6), 1511–1521. https://doi.org/10.1029/WR007i006p01511.

Gelhar, L.W., Welty, C., Rehfeldt, K.R., 1992. A critical review of data on field-scale dispersion in aquifers. Water Resour. Res. 28 (7), 1955–1974. https://doi.org/10.1029/92WR00607.

Harbaugh, A.W., Banta, E.R., Hill, M.C., & McDonald, M.G. (2000). MODFLOW-2000, the US Geological survey modular ground-water model—User guide to modularization concepts and the ground-water flow process Virginia: US Geological Survey.

Hellström, G., Tsang, C.-F., Claesson, J., 1988a. Buoyancy flow at a two-fluid interface in a porous medium: analytical studies. Water Resour. Res. 24 (4), 493–506. https://doi.org/10.1029/WR024i004p00493.

Hellström, G., Tsang, C.-F., Claesson, J., 1988b. Combined forced-convection and buoyancy flow at a two-fluid interface in a porous medium: analytical studies. Water Resour. Res. 24 (4), 507–515. https://doi.org/10.1029/WR024i004p00507.

Henry, A., Prasher, R., Majumdar, A., 2020. Five thermal energy grand challenges for decarbonization. Nat. Energy 5 (9), 635–637. https://doi.org/10.1038/s41560-020-0675-9.

Houben, G., 2015. Review: hydraulics of water wells—flow laws and influence of geometry. Hydrogeol. J. 1–25. https://doi.org/10.1007/s10040-015-1312-8.

Huysmans, M., Dassargues, A., 2005. Review of the use of Péclet numbers to determine the relative importance of advection and diffusion in low permeability environments. Hydrogeol. J. 13 (5), 895–904. https://doi.org/10.1007/s10040-004-0387-4.

IEA. (2019). *Renewables 2019 - Analysis and forecast to 2024*. Retrieved from https://iea.blob.core.windows.net/assets/a846e5cf-ca7d-4a1f-a81b-ba1499f2cc07/Renewables_2019.pdf.

Kallesøe, A.J., & Vangkilde-Pedersen, T. (2019). *Underground Thermal Energy Storage (UTES) – state-of-the-art, example cases and lessons learned.* Retrieved from https://www.heatstore.eu/documents/HEATSTORE_UTES%20State%20of%20the%20Art_WP1_D1.1_Final_2019.04.26.pdf.

Lake, L.W., 1988. The origins of anisotropy. J. Pet. Technol. 40 (04), 395–396. https://doi.org/10.2118/17652-PA.

Langevin, C. (2009). *SEAWAT: a Computer Program for Simulation of Variable-Density Groundwater Flow and Multi-Species Solute and Heat Transport* (2009-3047). Retrieved from https://pubs.usgs.gov/tm/tm6a22/.

Langevin, C.D., 2008. Modeling axisymmetric flow and transport. Groundwater 46 (4), 579–590. https://doi.org/10.1111/j.1745-6584.2008.00445.x.

Langevin, C.D., Thorne, D.T., Dausman, A.M., Sukop, M.C., & Guo, W. (2008). *SEAWAT Version 4: a computer program for simulation of multi-Species Solute and heat transport.* Retrieved from Reston, Virginia.

Maier, R., Leven, C., Sánchez-León, E., Strasser, D., Stoll, M., Cirpka, O.A., 2022. Revealing vertical aquifer heterogeneity and hydraulic anisotropy by pumping partially penetrating wells. Hydrogeol. J. 30 (2), 463–477. https://doi.org/10.1007/s10040-022-02458-9.

Mindel, J.E., Alt-Epping, P., Landes, A.A.L., Beernink, S., Birdsell, D.T., Bloemendal, M., Driesner, T., 2021. Benchmark study of simulators for thermo-hydraulic modelling of low enthalpy geothermal processes. Geothermics 96, 102130. https://doi.org/10.1016/j.geothermics.2021.102130.

Rau, G.C., Andersen, M.S., Acworth, R.I., 2012. Experimental investigation of the thermal dispersivity term and its significance in the heat transport equation for flow in sediments. Water Resour. Res. 48 (3), 1–21. https://doi.org/10.1029/2011WR011038.

Scheidegger, A.E., 1961. General theory of dispersion in porous media. J. Geophys. Res. (1896-1977) 66 (10), 3273–3278. https://doi.org/10.1029/JZ066i010p03273.

Schout, G., Drijver, B., Gutierrez-Neri, M., Schotting, R., 2014. Analysis of recovery efficiency in high-temperature aquifer thermal energy storage: a Rayleigh-based

method. Hydrogeol. J. 22 (1), 281–291. https://doi.org/10.1007/s10040-013-1050-8.

Sharqawy, M.H., Lienhard, J.H., Zubair, S.M., 2012. Thermophysical properties of seawater: a review of existing correlations and data. Desalination Water Treat. 16 (1–3), 354–380. https://doi.org/10.5004/dwt.2010.1079.

Sheldon, H.A., Wilkins, A., Green, C.P., 2021. Recovery efficiency in high-temperature aquifer thermal energy storage systems. Geothermics 96, 1–18. https://doi.org/10.1016/j.geothermics.2021.102173.

Sommer, W., Valstar, J., van Gaans, P., Grotenhuis, T., Rijnaarts, H., 2013. The impact of aquifer heterogeneity on the performance of aquifer thermal energy storage. Water Resour. Res. 49 (12), 8128–8138. https://doi.org/10.1002/2013wr013677.

Sommer, W.T., Doornenbal, P.J., Drijver, B.C., van Gaans, P.F.M., Leusbrock, I., Grotenhuis, J.T.C., Rijnaarts, H.H.M., 2014. Thermal performance and heat transport in aquifer thermal energy storage. Hydrogeol. J. 22 (1), 263–279. https://doi.org/10.1007/s10040-013-1066-0.

Tang, D.W.S., van der Zee, S.E.A.T.M., 2021. Dispersion and recovery of solutes and heat under cyclic radial advection. J. Hydrol. (Amst.) 602, 1–16. https://doi.org/10.1016/j.jhydrol.2021.126713.

Ürge-Vorsatz, D., Cabeza, L.F., Serrano, S., Barreneche, C., Petrichenko, K., 2015. Heating and cooling energy trends and drivers in buildings. Renew. Sustain. Energy Rev. 41, 85–98. https://doi.org/10.1016/j.rser.2014.08.039.

van Beek, C.G.E.M., Breedveld, R.J.M., Juhász-Holterman, M., Oosterhof, A., Stuyfzand, P.J., 2009. Cause and prevention of well bore clogging by particles. Hydrogeol. J. 17 (8), 1877–1886. https://doi.org/10.1007/s10040-009-0537-9.

van der Roest, E., Beernink, S., Hartog, N., van der Hoek, J.P., Bloemendal, M., 2021. Towards sustainable heat supply with decentralized multi-energy systems by integration of subsurface seasonal heat storage. Energies 14 (23), 1–31. https://doi.org/10.3390/en14237958.

van Lopik, J.H., Hartog, N., Zaadnoordijk, W.J., 2016. The use of salinity contrast for density difference compensation to improve the thermal recovery efficiency in high-temperature aquifer thermal energy storage systems. Hydrogeol. J. 24 (5), 1255–1271. https://doi.org/10.1007/s10040-016-1366-2.

Vandenbohede, A., Louwyck, A., Vlamynck, N., 2014. SEAWAT-based simulation of axisymmetric heat transport. Groundwater 52 (6), 908–915. https://doi.org/10.1111/gwat.12137.

Voss, C.I. (1984). *A finite-element simulation model for saturated-unsaturated, fluid-density-dependent groundwater flow with energy transport or chemically reactive single-species solute ransport.* Retrieved from Reston, Virginia.

Weatherill, D., Simmons, C.T., Voss, C.I., Robinson, N.I., 2004. Testing density-dependent groundwater models: two-dimensional steady state unstable convection in infinite, finite and inclined porous layers. Adv. Water Resour. 27 (5), 547–562. https://doi.org/10.1016/j.advwatres.2004.01.003.

Wesselink, M., Liu, W., Koornneef, J., van den Broek, M, 2018. Conceptual market potential framework of high temperature aquifer thermal energy storage - a case study in the Netherlands. Energy 147, 477–489. https://doi.org/10.1016/j.energy.2018.01.072.

Xynogalou, M., 2015. MSc. Delft University of Technology, Delft.

Zech, A., Attinger, S., Bellin, A., Cvetkovic, V., Dagan, G., Dietrich, P., Teutsch, G., 2022. Evidence based estimation of macrodispersivity for groundwater transport applications. Groundwater 61 (3), 346–362. https://doi.org/10.1111/gwat.13252.

Zheng, C., & Wang, P.P. (1999). *MT3DMS: a Modular Three-Dimensional Multispecies Transport Model for Simulation of Advection, Dispersion, and Chemical Reactions of Contaminants in Groundwater Systems; Documentation and User's Guide.*